Network connectivity and local transcriptomic vulnerability underpin cortical atrophy progression in Parkinson's disease

Running head: Cortical atrophy progression in Parkinson's disease

Andrew Vo[1], Christina Tremblay[1], Shady Rahayel[1,2], Golia Shafiei[3], Justine Y. Hansen[1], Yvonne Yau[1], Bratislav Misic[1], Alain Dagher[1]*

[1] Montreal Neurological Institute, McGill University, Montreal, Canada

[2] Centre for Advanced Research in Sleep Medicine, Hôpital du Sacré-Cœur de Montréal, Montreal, Canada

[3]Department of Psychiatry, Perelman School of Medicine, University of Pennsylvania, Philadelphia, PA 19104, USA

*Corresponding Author Information:

Alain Dagher (email: alain.dagher@mcgill.ca)

Abstract

Parkinson's disease pathology is hypothesized to spread through the brain via global connections between regions and local vulnerabilities within those regions. The resulting changes to brain morphology have previously been demonstrated in both prodromal and *de novo* Parkinson's disease. However, it remains unclear whether the longitudinal progression pattern of atrophy in Parkinson's disease is similarly explained by network spreading and selective vulnerability. We address this gap by mapping the trajectory of cortical atrophy rates in a large, multi-centre cohort of Parkinson's disease patients and related this atrophy progression pattern to network architecture and gene expression profiles. Across 4-year follow-up visits, increased atrophy rates were observed in posterior, temporal, and superior frontal cortices. We demonstrated that this progression pattern was shaped by network connectivity. Regional atrophy rates were strongly related to neighbourhood atrophy rates across structurally and functionally connected regions. We also found that atrophy progression was associated with specific gene expression profiles. The genes most related to atrophy rates were those enriched for mitochondrial and metabolic function. Taken together, our findings demonstrate that both global and local brain features influence vulnerability to neurodegeneration in Parkinson's disease.

Key Words: Parkinson's disease, structural MRI, cortical thinning, connectomics, imaging transcriptomics

Introduction

Structural brain changes are observed in Parkinson's disease (PD).[1–3] The spatial topography of disease-related atrophy is not uniform across the cortex, however. Some regions appear to be more vulnerable to disease pathology than others, but the brain features that may determine this atrophic pattern and its progression are not entirely clear. One possibility is that PD occurs through a network spreading process. Early proposals by Braak et al.,[4,5] described a spatiotemporal distribution of Lewy pathology in post-mortem samples that followed a stereotyped caudal-to-rostral gradient. Pathology appeared first in the dorsal motor nucleus of the vagus in the lower brainstem, then progressed to the midbrain coinciding with the onset of motor symptoms that typify PD, before reaching subcortical and cortical areas. This pattern of disease spread appears to reflect brain network organization, suggesting that PD might target large-scale intrinsic networks.[6,7]

Recent evidence involving alpha-synuclein fibrils injected in mice further supports the theory that PD pathology propagates via neuronal connections.[8–10] MRI studies in PD patients are also consistent with a network spreading model. Brain atrophy in PD measured with deformation-based morphometry was found to correlate with connectivity to the substantia nigra, a presumed disease epicenter.[2] Cortical thinning in PD was associated with structural and functional connectivity to a subcortical "disease reservoir".[11] However, the observed pathology distribution in PD does not always fit the pattern originally described by Braak's staging model,[12] which suggests that factors other than or in addition to network connectivity may shape the disease pattern.

One such factor might be the selective vulnerability of certain regions to PD pathology,[13,14] which can be conferred by local features such as cellular composition,[15] neuroreceptor profiles,[16] and gene expression.[17] For example, variations in regional alpha-synuclein protein expression have been shown to produce differences in vulnerability to neurodegeneration.[18] Agent-based simulations of alpha-synuclein spread in PD through the connectome also showed that incorporation of local differences in gene expression related to protein synthesis and degradation improved the *in silico* recreation of brain atrophy, suggesting a crucial involvement of regional gene expression in shaping disease propagation.[19–21] Indeed, the underlying factors that shape the atrophy pattern PD are complex and multifactorial, requiring further investigation.

In the present study, we aimed to characterize the network connectivity and local gene expression features underpinning the pattern of cortical atrophy progression in PD. We first charted the trajectory

of cortical atrophy using the Parkinson Progression Marker Initiative (PPMI)[22], a large, multi-centre cohort of *de novo* PD patients followed longitudinally up to 4 years after diagnosis. We then explored whether the cortical atrophy progression pattern mapped onto specific functional networks, cytoarchitectonic classes, cellular distributions, and neurotransmitter systems. Next, we applied a network spreading model[23,24] to examine whether network connectivity constrained the atrophy progression pattern in PD. Finally, we investigated the gene expression profiles associated with cortical atrophy progression in PD and its transcriptional relevance in terms of biological processes.

Methods

Participants

Demographic, clinical, and MRI data were downloaded from the PPMI (http://www.ppmi-info.org).[22] All participating sites received approval from their local research ethics committee. Informed consent was obtained from all participants in accordance with the Declaration of Helsinki.[25] PD patients met the inclusion criteria outlined by the PPMI. Healthy controls were free of neurological disease. For participants with available 3T MRI data, only PD patients with a minimum of two visits and healthy controls with a baseline (due to limited longitudinal imaging in this group) were included in the present study.

Cortical thickness analysis

T1-weighted MRI scans were acquired following standardized procedures and acquisition parameters (http://www.ppmi-info.org/study-design/research-documents-and-sops/). We used the CIVET 2.1.1 pipeline (http://www.bic.mni.mcgill.ca/ServicesSoftware/CIVET) to generate cortical thickness models for PD patients across follow-up visits and healthy controls at baseline.[26] Briefly, T1-weighted MRIs were linearly transformed to the MNI-ICBM152 volumetric template, corrected for signal intensity non-uniformity, and segmented into grey matter, white matter, CSF, and background.[26–28] The grey and white matter surface boundary was fitted across 40,692 vertices in each hemisphere (inner cortical surface) and expanded to fit the grey matter and CSF boundary (outer cortical surface) using a fully automated method (Constrained Laplacian Anatomic Segmentation using Proximity algorithm).[29] Cortical thickness at each of 81,920 vertices was measured as the linked distance between corresponding inner and outer surface vertices in mm. Quality control of the resulting outputs was carried out by two independent reviewers and only scans with consensus of the two reviewers were retained for further analysis. 146 of

the 624 PD and 57 of the 194 HC scans failed quality control. Reasons for exclusion included: motion artifacts, low signal-to-noise ratio, artifacts due to hyperintensities from blood vessels, surface-surface intersections, and/or poor grey and white matter segmentation.

To control for normal age- and sex-related effects on cortical thickness, we generated W-score maps for each PD patient at each follow-up visit. W-scoring is comparable to z-scoring but allows for the combined adjustment of many specific covariates.[30] Vertex-wise linear regressions were first performed in healthy controls between age, sex, and cortical thickness. W-score maps were then computed in PD patients using the following formula:

$$W_i = \frac{raw\ thickness_i - \exp thickness_i}{SD_{res}}$$

where W_i is the W-score at vertex *i*, $raw\ thickness_i$ is the raw cortical thickness in PD measured at vertex *i*, $exp\ thickness_i$ is the expected cortical thickness in healthy controls at vertex *i* given the patient's age and sex ($thickness \sim AGE + SEX$), and SD_{res} is the standard deviation of the residuals in healthy controls. Note that data from healthy controls at baseline were used as the reference because only a limited number had longitudinal MRI data available. For interpretability, W-scores were inverted such that more positive scores indicated greater atrophy rates whereas more negative scores denoted lower atrophy rates. These W-scored maps were used to model cortical atrophy rates with linear mixed effects.

Cortical atrophy maps were parcellated into equally sized regions (or parcels) using a multi-scale edition of the Desikan-Killiany atlas[31] referred to here as the "Cammoun atlas".[32] Parcellation resolutions spanned 68, 114, 219, 448, and 1000 cortical regions. Parcel-wise values were calculated as the mean value of all vertices assigned to a given parcel according to the Cammoun atlas. We repeated analyses at different parcellation resolutions to ensure results were replicable and robust to the choice of spatial scale.

Cortical atrophy progression analysis

W-scored vertex-wise cortical thickness values were averaged for the whole-brain as well as within parcels according to the Cammoun atlas.[32] Linear mixed effects models were used to examine the change in cortical thickness across follow-up visits. Time since baseline visit (years) was used as a fixed effect of interest.[33] Subject-wise slope and intercept were modeled as random effects. Separate models

were fitted for each parcel and results were corrected for multiple comparisons using false discovery rate (FDR)-correction with $p < 0.05$ indicating statistical significance.

$$thickness \sim 1 + TIME + SITE + (TIME|SUBJ)$$

The resulting *t*-statistic map corresponding to the effect of time on cortical thickness in PD was used as a measure of atrophy progression in all subsequent analyses.

Clinical variable progression analysis

Analogous to our cortical atrophy progression analysis, we performed linear mixed effects modeling on longitudinal clinical variable data in PD patients. The full list of clinical variables is reported in Table 1. Imputation of missing scores (7.6%) was performed through replacement with the group mean at each time point. Separate models were fitted for each clinical outcome, with time since baseline visit (years), adjusted for age, sex, and education as fixed effects. Subject-specific slope and intercept were modeled as random effects. Results were FDR-corrected for multiple comparisons using a threshold of $p < 0.05$.

$$clinical\ variable \sim 1 + TIME + AGE + SEX + EDUCATION + SITE + (TIME|SUBJ)$$

Atrophy-clinical progression relationship

Behavioural partial least squares (PLS) analysis is a multivariate approach that identifies latent variables that explain the maximum covariance between two datasets.[34,35] Here, we related a regional atrophy progression matrix $\boldsymbol{X}_{n\times p}$ (160 patients × 68 regions) with a clinical progression matrix $\boldsymbol{Y}_{n\times q}$ (160 patients × 25 clinical outcomes). The matrices were first z-scored column-wise and used to generate an atrophy-clinical covariance matrix $\boldsymbol{R}_{q\times p} = \boldsymbol{Y'X}$. This covariance matrix was then subjected to singular value decomposition (SVD)[36] such that $\boldsymbol{R} = \boldsymbol{USV'}$ where $\boldsymbol{U}_{p\times l}$ and $\boldsymbol{V}_{q\times l}$ are orthogonal matrices of left and right singular values and $\boldsymbol{S}_{l\times l}$ is a diagonal matrix of singular values. Each latent variable *i* was comprised of the *i*th columns of $\boldsymbol{U}$ and $\boldsymbol{V}$ and the covariance between these singular vectors was represented by the *i*th element of $\boldsymbol{S}$. Left singular vectors of $\boldsymbol{U}$ represented the degree to which each brain region contributed to a latent variable (i.e., brain weight) whereas right singular vectors of $\boldsymbol{V}$ represented the degree to which clinical outcomes contributed to the same latent variable (i.e., clinical weight). Positively weighted brain regions covaried with positively weighted clinical outcomes and negatively weighted brain regions covaried with negatively weighted clinical outcomes. Pearson correlation tested the relationship between regional brain weights and atrophy rates, with a positive correlation indicating more positively

weighted brain regions were associated with greater cortical atrophy progression. The effect size (η) associated with a given latent variable was estimated as the ratio of the squared singular value (σ) to the sum of all squared singular values. SVD generates the same number of latent variables as the rank of the covariance matrix ***R*** (i.e., 25).

Permutation tests were used to evaluate the statistical significance of each latent variable; that is, whether the variance explained was significantly greater than what would be expected by a null. Rows of matrix ***X*** were randomly reordered to generate a covariance matrix **R** from the permuted matrix **X** and original matrix **Y** before applying SVD. This procedure was repeated 5,000 times to generate a null distribution of singular values to which the original singular value was compared. Bootstrap resampling was then used to estimate the contribution and reliability of individual variables (i.e., brain regions and clinical outcomes) to each latent variable. The rows of both matrices ***X*** and ***Y*** were randomly selected with replacement to generate a resampled covariation matrix **R** that was subjected to SVD. This procedure was repeated 5,000 times to generate a sampling distribution for each weight in the singular vectors **U** and **V**. For each singular vector, a bootstrap ratio was calculated as the ratio of each singular vector to its bootstrap-estimated standard error. Thus, individual variables with larger bootstrap ratios had larger weights (i.e., contributed greatly to the multivariate pattern) and smaller standard errors (i.e., were more reliable).

Null models

"Spin tests"[37,38], or spatial autocorrelation-preserving null model testing, were used to assess the statistical significance whenever examining the correspondence between topologies of two brain maps. Given that neighbouring brain regions are not statistically independent and instead demonstrate a high degree of autocorrelation, null models that preserve this spatial autocorrelation of brain maps allow for more accurate inferences of the underlying data.[38] Null models were generated using the *netneurotools* toolbox.[38] Briefly, each parcel of the Cammoun atlas registered on the FreeSurfer fsaverage surface space was assigned the spatial coordinate of the vertex on an fsaverage spherical projection that was closest to its center of mass. The spatial coordinates were then randomly rotated for one hemisphere and mirrored to the other hemisphere. Lastly, each original parcel was reassigned the value of the closest rotated parcel. This procedure was repeated 10,000 times to generate a spatial autocorrelation-preserving null distribution against which empirical observations could be benchmarked.[39]

Spatial overlap between regional atrophy rates and local brain features

We tested if the atrophy rate pattern was associated with specific brain features such as intrinsic networks[40], tissue cytoarchitectonic classes[41,42], cell type distributions[43,44], and neurotransmitter receptor and transporter densities.[45,46] The Yeo intrinsic networks[40] classify brain regions as one of seven resting state networks (visual, sensorimotor, dorsal attention, ventral attention, limbic, frontoparietal, and default mode) and the von Economo cytoarchitectonic classes[42] label brain regions as one of seven laminar cortical types (primary motor, association 1/2, primary/secondary sensory, primary sensory, limbic, and insular). We calculated the mean atrophy progression for each intrinsic network and cytoarchitectonic class and compared these empirical means to null mean distributions generated from spatial autocorrelation-preserving null models to determine their statistical significance.

For cell type distributions, we correlated the atrophy rate pattern with the gene expression maps of seven different cell classes including: astrocytes, endothelial cells, excitatory and inhibitory neurons, microglia, oligodendrocytes, and oligodendrocyte precursors. Each cell class was first associated with a gene list derived from single-cell RNA sequencing studies of post-mortem human cortical samples.[43] The spatial expression patterns of each gene list were generated and parcellated to the Cammoun atlas using post-mortem brain data from the AHBA[47] and the *abagen* toolbox[48] based on recommendations outlined by Arnatkeviciute et al.[49] Pearson correlations compared regional atrophy rates to gene expression patterns for each of the seven cell classes. These correlations were tested against spatial autocorrelation-preserving null models.[37,38]

Finally, we compared the atrophy rate pattern to maps of different neurotransmitter receptor and transporter densities derived from PET imaging of more than 1,200 total individuals.[45] These 19 receptors and transporters spanning nine neurotransmitter systems included: acetylcholine ($\alpha_4\beta_2$, M_1, VAChT), cannabinoid (CB_1), dopamine (D_1, D_2, DAT), GABA ($GABA_{A/BZ}$), histamine (H_3), glutamate ($mGluR_5$, NMDA), norepinephrine (NET), opioid (MOR), and serotonin (5-HT_{1A}, 5-HT_{1B}, 5-HT_{2A}, 5-HT_4, 5-HT_6, 5-HTT). Volumetric tracer maps were obtained from https://github.com/netneurolab/hansen_receptors, parcellated to the Cammoun atlas (at the three lowest parcellation resolutions due to map availability) and individually z-scored using the *neuromaps* toolbox[45]. Tracers for which multiple density maps were available were combined using weighted averaging. Pearson correlations compared regional atrophy rates to receptor/transporter expression and were tested against spatial autocorrelation-preserving null models.[37,38]

Lastly, we tested if there was baseline and progression of asymmetry in cortical thickness between hemispheres. For each PD patient, mean cortical thickness was calculated in each hemisphere and an asymmetry index was computed based on the following formula:

$$AI = \frac{left - right}{(left + right)}$$

with more positive scores reflecting greater left dominance and more negative scores denoting greater right dominance. Asymmetry index scores were submitted to a linear mixed effects model to examine the change in cortical thickness asymmetry across follow-up visits.

Structural and functional networks

Structural and functional data from 70 healthy young adults (25.3 ± 4.9 years; 16 females) were obtained from the publicly available Lausanne dataset.[50] Imaging was acquired in a 3T MRI scanner (Trio, Siemens Medical) with a 32-channel head coil. Acquisition parameters and preprocessing steps are described in greater detail elsewhere.[50]

Diffusion spectrum imaging (128 diffusion-weighted volumes and a single b_0 volume, maximum b-value = 8,000 s/mm^2, voxel size = 2.2 × 2.2 × 3.0 mm) was analyzed with deterministic streamline tractography to generate individual structural connectivity networks. These networks were parcellated according to the Cammoun atlas. A binary group-consensus structural network was created using an approach that preserved the density and edge-length distributions of individual connectomes.[51] A weighted structural network was then generated by weighting edges in the binary network by the log-transform of non-zero fiber density, scaled to values between 0 and 1.

Resting-state MRI data was acquired with a gradient echo EPI sequence sensitive to blood-oxygen-level-dependent (BOLD) contrast (3.3 mm in-plane resolution and slice thickness with 0.3 mm gap, TR = 1920 ms, 280 volumes). Time series data were parcellated according to the Cammoun atlas. Pairwise Pearson correlations were used to estimate individual functional connectivity networks. A group-average functional network was constructed as the mean pairwise connectivity across individuals. One individual did not have fMRI data and therefore the functional network was derived from n = 69 participants.

Network spreading analysis

Next, we related the atrophy progression pattern to brain connectivity using a network spreading approach.[24] For each region (or node), we calculated a neighbourhood atrophy rate. This score described the mean atrophy rate across anatomically connected neighbours weighted by the strength of connectivity. Connectivity was defined using structural and functional reference networks derived from a separate cohort of healthy participants (see "Structural and functional networks"). Neighbourhood atrophy rate was calculated as follows:

$$A_i = \frac{1}{N_i}\sum_{j=1}^{N_i} a_j \times conn_{ij} \quad , \quad j \neq i$$

where A_i is the average neighbour atrophy rate of node i, a_j is the atrophy rate of the j-th neighbour of node i, $conn_{ij}$ is the strength of connection between nodes i and j, and N_i is the total number of neighbours that are structurally connected to node i (i.e., node degree). Neighbour atrophy rate is made independent from node degree by normalization with term N_i. For a given node, a neighbour was defined as another structurally connected node. Self-connections of a node and itself were excluded ($j \neq i$). Connectivity ($conn_{ij}$) was defined either structurally or functionally in separate analyses.

Pearson correlations tested the relationship between the atrophy rate of each node with that of its neighbourhood and compared against spatial autocorrelation-preserving null models.[37,38] We also examined the importance of structural and functional connectivity to node-neighbour correlations by comparing connected versus not-connected neighbours using Fisher's *z* tests.

Gene expression

To understand the gene expression profiles underpinning cortical atrophy progression patterns, regional gene expression data were obtained from the Allen Human Brain Atlas (AHBA)[47] dataset and processed with the *abagen* toolbox.[48] The AHBA is a comprehensive atlas of microarray data from six post-mortem brains (1 female, mean age = 42.5 ± 13.4 years). Microarray probes were first reannotated following previous recommendations.[49] Only those probes with a signal-to-noise ratio relative to background of greater than 50% were retained. When multiple probes indexed expression of the same gene, the one with the most consistent pattern of regional variation across donors was selected. This procedure resulted in 15,633 total genes being retained. Samples were assigned to parcels according to the Cammoun atlas. To increase spatial coverage, tissue samples were mirrored bilaterally across the left and right hemisphere.[52–54] When a sample was not found directly within a parcel, the nearest sample (up

to a 2 mm distance) was selected. If no samples were found within 2 mm of a parcel, the sample closest to the centroid of the empty parcel across all donors was selected. This sample-to-region matching was restricted to each hemisphere and within gross structural divisions (i.e., cortex, subcortex/brainstem, and cerebellum) to minimize the potential for misassignment. Samples without an assignment were discarded. Expression values were normalized across genes using a scaled robust sigmoid function[55] and rescaled to the unit interval. Microarray samples belonging to the same parcels were aggregated by computing the mean expression across samples for the individual parcels, for each donor. Finally, regional expression profiles were averaged across donors to construct a region × gene expression matrix that was submitted to a PLS regression.

Gene set enrichment analysis

We used PLS analysis to uncover the gene expression profiles that predicted atrophy progression in PD. Latent variables that explained the maximum covariance between predictor matrix ***X*** (68 regions × 15,633 genes) and matrix ***Y*** (68 region × 1 atrophy rate) were identified. To determine the statistical significance of components (i.e., that the variance explained was greater than expected by a null), empirical variance was tested against the variance observed in 10,000 spatial autocorrelation-preserving null models. The contribution of genes to each component was measured using bootstrap resampling. Rows in ***X*** and ***Y*** matrices were randomly shuffled and PLS regression was repeated 5,000 times to generate a null distribution and estimate standard errors for each gene. Bootstrap ratios were calculated as the ratio of each gene expression weight to its bootstrapped-estimated standard error. Genes with large bootstrap ratios contributed greatly to the latent variable and were more reliable. Genes lists were ordered according to their bootstrap ratios and this ranked list was entered into a gene set enrichment analysis (GSEA).

GSEA, performed on the WebGestalt platform (http://www.webgestalt.org)[56] with the Gene Ontology knowledge base (http://geneontology.org), was used to explore the biological processes enriched in the gene expression profiles associated with atrophy rates in PD. This analysis tested whether the most positively and negatively weighted genes in the ranked list occurred more frequently than expected by chance.[57] The minimum and maximum number of genes for enrichment was set to 3 and 2,000, respectively. Results were FDR-corrected for multiple comparisons using 1,000 random permutations. Only the top 10 most significant positively and negatively weighted terms were interpreted.

Data availability

Clinical and imaging data used in this study are part of the PPMI database and can be accessed at http://www.ppmi-info.org/data. All other datasets and analysis tools along with their sources are cited in the "Methods" section.

Results

Participants

After completing quality control of the cortical thickness maps, the final sample was comprised of 160 patients contributing 478 scans (151 at baseline, 121 at year-1, 114 at year-2, and 82 at year-4) and 137 healthy controls at baseline. The two groups were similar to one another at baseline in terms of age (PD = 61.1 ± 9.8 years, HC = 59.9 ± 11.4 years; $t(286) = 0.97$, $p = 0.37$) and sex ($\chi^2 = 0.25$, $p = 0.61$). Table 1 displays demographic and clinical measure scores for PD patients included in the present study. Linear mixed effects models of clinical progression in PD patients revealed a significant effect of time for measures of disease stage (i.e., Hoehn & Yahr score), motor symptoms (i.e., MDS-UPDRS-II, MDS-UPDRS-III, tremor, rigidity), non-motor symptoms (e.g., MDS-UDPRS-I, Scales for Outcomes in Parkinson's Disease-Autonomic, REM sleep behavior disorder, phonemic fluency), and CSF protein levels (amyloid beta, phosphorylated and total tau, NfL). Generally, these results reflected a worsening of clinical symptoms over time except for phonemic fluency, which improved across visits. Whereas amyloid beta, phosphorylated tau, and total tau levels in CSF reduced over time, NfL levels increased.

Longitudinal changes in cortical atrophy

Linear mixed effects models of whole-brain cortical thickness revealed a significant effect of time ($t = 4.955$, $p < 0.001$) reflecting increased atrophy across visits. Region-wise analysis of cortical thickness showed a largely posterior parietal, temporal, and superior frontal pattern of atrophy progression (Fig. 1a). No regions showed statistically significant increases in cortical thickness over time (Fig. 1b). The spatial pattern of atrophy progression observed was consistent across parcellation resolutions (Fig. S1). Overall, we observed a widespread pattern of longitudinal cortical atrophy progression in PD patients.

Atrophy-clinical progression

PLS was used to relate changes in atrophy and clinical outcome progression. We identified the first latent variable that accounted for 49.1% ($p < 0.001$) of the covariance between these measures. Regional brain weights associated with this latent variable were positively correlated with atrophy rates

(r = 0.309, p_{spin} = 0.028; Fig. 2b), such that brain regions with more positive weighting on the latent variable also demonstrated greater atrophy progression (Fig. 2a). Of the 25 longitudinal clinical measures included in the analysis, 12 measures significantly contributed to the latent variable (Fig. 2c), namely visuospatial perception from the Benton Judgement of Line Orientation test, psychomotor slowing from Symbol-Digit Modalities Test, Geriatric Depression Scale, Hoehn and Yahr disease stage, working memory from the Letter-Number Sequencing test, CSF levels of tau (phosphorylated and total tau) and NfL, the Questionnaire for Impulsive-Compulsive Disorders in Parkinson's Disease-Rating Scale, the Scales for Outcomes in Parkinson's Disease-Autonomic, MDS-UPDRS-I, and MDS-UPDRS-III.

Cortical atrophy progression is distributed within discrete brain systems

Spatial correspondence analyses tested whether the pattern of atrophy progression was pronounced in specific brain systems. Specifically, we examined the relationship between atrophy rates and the (i) Yeo intrinsic networks[40], (ii) von Economo cytoarchitectonic classes[42,58], (iii) cell type distributions, and (iv) neurotransmitter receptor and transporter densities[45]. Atrophy rates were relatively greater in the sensorimotor network (*mean* = 3.636, p_{spin} = 0.018; Fig. 3a) and relatively lesser in the ventral attention network (*mean* = 1.516, p_{spin} = 0.014; Fig. 3a). We also noted relatively greater atrophy rates within primary motor cortex (*mean* = 4.309, p_{spin} = 0.022; Fig. 3b). The atrophy progression pattern was negatively correlated with astrocyte cell distribution (r = -0.451, p_{spin} = 0.019; Fig. 3c). Regions with greater expression of astrocytes corresponded with relatively lower atrophy rates. Finally, atrophy progression was negatively correlated with the distribution of several receptors and transporters, including: 5HTT (r = -0.361, p_{spin} = 0.024), CB1 (r = -0.460, p_{spin} = 0.040), D1 (r = -0.604, p_{spin} <0.001), DAT (r = -0.470, p_{spin} = 0.001), H3 (r = -0.504, p_{spin} = 0.005), mGluR5 (r = -0.393, p_{spin} = 0.011), and MOR (r = -0.551, p_{spin} = 0.009). Atrophy progression was negatively correlated with each of these neurotransmitter systems (Fig. 3d), suggesting that regions with lower expression of these neuroreceptors displayed higher atrophy rates. Finally, cortical asymmetry was not found between left and right hemispheres at baseline (t = -0.764, p = 0.445) and did not progress across visits (t = -1.00, p = 0.317). Collectively, we found that the pattern of atrophy progression in PD is spatially distributed within discrete brain systems.

Structural and functional network connectivity constrains cortical atrophy progression

Using a network spreading approach (Fig. 4a)[24], we tested the relationship between the atrophy rate measured in each node and the mean atrophy rate across all structurally and functionally connected neighbours. We found positive correlations between node and neighbourhood atrophy rates (Fig. 4b),

suggesting regions with greater atrophy rates are themselves connected to neighbourhoods with overall greater atrophy rates. This was the case whether connectivity was defined structurally (r = 0.470, p_{spin} = 0.018; Fig. 4b left) or functionally (r = 0.425, p_{spin} = 0.049; Fig. 4b right). Importantly, these results were robust to different parcellation resolutions and when tested against spatial autocorrelation-preserving null models (Fig. S3).

We also considered node-neighbour relationships when networks were composed of connected versus not-connected neighbours. Fisher's z tests revealed that the magnitudes of correlations with connected neighbours were significantly greater than those for not-connected neighbours, whether defined structurally (z = 1.997, p = 0.046) or functionally (z = 2.427, p = 0.015; Fig. 3c). Node-neighbour correlations for structurally and functionally connected neighbours were significantly greater than not-connected neighbours across parcellation resolutions except at the highest spatial scale (i.e., 1000 regions; Fig. S3). Taken together, we demonstrate the influence of network architecture in shaping the pattern of cortical atrophy progression in PD.

Genes related to atrophy progression are enriched for mitochondrial and metabolic processes

PLS analysis was used to relate regional gene expression to the atrophy progression pattern in PD. The first (i.e., PLS1) and second (i.e., PLS2) significant latent variables explained 30.4% (p_{spin} = 0.027) and 26.8% (p_{spin} = 0.028) of the observed co-variance, respectively. Atrophy rates were positively correlated with brain weights that contributed to PLS1 (r = 0.540, p_{spin} = 0.012; Fig. 5a-b) and PLS2 (r = 0.519, p_{spin} < 0.001; Fig. 5d-e). In regions with greater atrophy rates, those genes that positively weighted on the latent variables were more expressed whereas those genes that negatively weighted on the latent variables were less expressed. Next, genes were ranked in order of their bootstrap ratios separately for each latent variable and examined for their biological relevance using GSEA. The most positively weighted genes (i.e., genes more expressed in regions with greater atrophy rates) were enriched for processes related mitochondrial and metabolic function (see Table S1 and S2). For genes positively associated with PLS1, the most enriched terms included "mitochondrial RNA metabolic process" (normalized enrichment score = 1.951, p_{FDR} = 0.037; Fig. 5c) and "mitochondrial gene expression" (normalized enrichment score = 1.889, p_{FDR} = 0.046; Fig. 5c). For genes positively related to PLS2, regions with greater atrophy rates had greater expression of genes involved in the "NADH dehydrogenase complex assembly" (normalized enrichment score = 1.967, p_{FDR} = 0.032; Fig. 5f) and "mitochondrial gene expression" (normalized enrichment score = 1.949, p_{FDR} = 0.024; Fig. 5f). Negatively weighted genes

associated with either latent variable was not found to be significantly enriched for specific biological processes. In summary, genes more expressed in regions with greater atrophy rates in PD are associated with mitochondria and metabolic functions.

Discussion

The present study aimed to characterize and better understand the progression of cortical atrophy in early PD. We found that cortical atrophy progresses in regions within posterior, temporal, and superior frontal cortices over 4 years. We also found the progression of cortical atrophy occurred in association with the clinical progression of motor, non-motor, and CSF measures. Moreover, we demonstrated that cortical atrophy progression in PD is underpinned by specific connectivity and gene expression features. Specifically, we showed that network architecture significantly constrains the progression of cortical atrophy and that this pattern overlapped with motor network and tissue classes, astrocyte distributions, and several neurochemical distributions. In addition, cortical atrophy progression was related to gene expression profiles enriched for mitochondrial and metabolic functions. Taken together, our results shed light on the global network and local features that shape disease progression in PD.

Cortical atrophy and clinical outcome progression

We observed progression of cortical atrophy in PD within posterior, temporal, and superior frontal cortices. Cortical thickness is thought to represent the volume of neuropil—the axons, dendrites, and synapses within cortical columns—and therefore cortical thinning likely reflects the loss of neuropil and the synaptic density.[59] The observed pattern was largely consistent with that found in case-control[60–63] and longitudinal[1,11,64–66] studies of PD. Along with regional atrophy progression, worsening clinical outcomes were also found in several motor (i.e., H&Y stage, UPDRS-II, UPDRS-III), non-motor (i.e., UPDRS-I, RBDSQ, SCOPA-AUT), and CSF (i.e., beta-amyloid, p-tau, t-tau, NfL) measures. Worsening motor symptoms and autonomic dysfunction is expected with advancing disease.[67,68] Although measures of verbal fluency were found to improve with time, this likely reflects either practice or medication effects.

A multivariate analysis identified a single latent variable that explained the covariance between the progressions of cortical atrophy and clinical outcomes in this PD cohort. The clinical measures that significantly contributed to this latent variable included motor (i.e., H&Y stage, UPDRS-III), non-motor (i.e., psychomotor slowing, depression, compulsive-impulsive behaviours, autonomic function, UPDRS-I),

and CSF biomarkers (i.e., t-tau, p-tau, and NfL levels). These findings are in line with a PLS analysis performed on whole-brain atrophy and clinical data in *de novo* PD patients at baseline, which uncovered a clinical phenotype that included both motor and non-motor features associated with diffuse tissue loss.[69]

We also observed longitudinal changes in several CSF biomarkers, including decreases in tau (p-tau and t-tau) and beta-amyloid but increases in NfL levels. Although both CSF tau and beta-amyloid are markers of Alzheimer's disease, many PD patients demonstrate co-pathologies that correlate with cognitive decline and reduced survival.[70] Longitudinal modeling of these CSF biomarkers in PD is limited, however a recent study performed on the PPMI cohort found decreasing levels of p-tau and beta-amyloid in PD patients compared to healthy controls[71], a trend with which our results are in line. Lastly, there was a noted elevation in NfL concentrations in CSF over time. Neurofilaments are cytoskeletal components of myelinated axons that are released following axonal degeneration.[72] Of the several subclasses of neurofilaments, NfL is the most thoroughly investigated as a biomarker of PD progression.[73,74] Studies have shown that NfL levels in blood and CSF are significantly elevated in PD patients compared to healthy controls, and baseline NfL levels are predictive of motor and cognitive progression in PD.[75–78] Here we add to this literature by showing progressive increases in NfL covarying with regional cortical atrophy rates.

Distribution of cortical atrophy progression

The atrophy progression pattern was found to be localized to specific brain systems. Relatively greater atrophy rates were observed in sensorimotor network and primary motor cortex, whereas relatively lower atrophy rates were found in ventral attention network. Motor and sensory areas of the cortex are primarily connected to the putamen, which is severely dopamine-depleted in PD.[79] Previous work has shown that cortical thinning is determined by connectivity to a subcortical "disease reservoir" in PD, suggesting a potential pathway by which PD pathology might dominate specific regions or networks of neocortex.[11]

Additionally, regions with higher expression of astrocytes corresponded to regions with lower atrophy rates. Whether the role of astrocytes in PD is deleterious or protective has yet to be settled.[80] For example, some evidence suggests that alpha-synuclein aggregates readily exchanged between neurons and astrocytes produce an inflammatory response and lead to neuronal death if transferred from astrocytes to neurons.[81,82] In contrast, others have shown that astrocytes may uptake and degrade

misfolded alpha-synuclein more efficiently than neurons.[83] This neuroprotective function seems in line with our observation of relatively less atrophy progression in astrocyte-rich regions, although more clarification is needed.

Finally, regions with higher atrophy rates overlapped areas with relatively lower distribution of several neurochemical systems including serotonin (5-HTT), cannabinoid (CB_1), dopamine (D_1, DAT), histamine (H_3), glutamate ($mGluR_5$), and opioid (MOR). The involvement of these various transmitters and receptors in PD pathology has been described previously and mapped to largely frontal and striatal regions.[84–88] Indeed, visual inspection of the cortical topography of these neurochemical maps (see Fig. S2) reveals their concentration in ventral frontal and limbic cortices, where we observed the lowest atrophy rates. Although we saw a negative association between atrophy rates and D_1/DAT concentrations (i.e., greater atrophy in regions with lower concentrations of dopamine receptor and transporter), note that our analysis was restricted to the cortical surface whereas dopamine deficiency caused by PD occurs primarily in subcortical regions.[89] Nonetheless, these results reveal interesting associations between PD-related atrophy and neurochemical mechanisms that warrant further exploration.

Network architecture shapes cortical atrophy progression

There is increasing evidence of a network spreading process of atrophy in multiple neurodegenerative diseases and psychiatric disorders, including PD, Alzheimer's disease, frontotemporal dementia, amyotrophic lateral sclerosis, and schizophrenia.[6,11,23,24,65,90–95] Although these diseases have distinct aetiologies, the fact that neurodegeneration follows large-scale brain networks raises the possibility of similar pathophysiological mechanisms. One hypothesis posits that neurodegenerative diseases spread through the cell-to-cell propagation of toxic agents in a prion-like manner.[7,96] In PD, that agent is a misfolded isoform of alpha-synuclein.[7,96,97]

We found evidence that cortical atrophy progression in PD is shaped by structural and functional networks. Regions with greater atrophy rates were more likely to be connected to neighbourhoods of regions with greater atrophy rates themselves. Intrinsic anatomical and functional connectivity was important for this model, as networks composed of not-connected nodes disrupted this region-neighbourhood relationship. Critically, we ensured our results were independent of spatial autocorrelation and were replicable across spatial scales. These findings replicate and extend previous work in support of a network spreading model in both prodromal[98] and incidental PD.[2,11,65,91,94,99]

Zeighami et al.[2] first showed in *de novo* PD patients that brain atrophy measured with deformation-based morphometry was associated with connectivity to the substantia nigra, a disease epicenter in PD. In a more recent study, Tremblay et al.[65] found that structural and functional connectivity continued to constrain deformation-based atrophy progression in PD patients followed longitudinally. Similarly, Yau et al.[11] reported that cortical thinning in *de novo* PD over a 1-year period was correlated with connectivity to a subcortical "disease reservoir". We build on these findings here by demonstrating the role of connectivity in the progression of cortical atrophy over a longer 4-year duration.

However, other pathogenic mechanisms would also follow the connectome. Connected areas tend to be similar in terms of cellular composition,[15] neuroreceptor profiles,[46] and gene expression.[17] Thus, a pathogenic process may target connected regions for reasons other than their connectivity. Highly connected hub regions in the brain tend to be targeted in almost all neurological diseases,[100] possibly because of their precarious energy needs. These regions also tend to be inter-connected.[101] Indeed, we previously showed that atrophy patterns in the PPMI dataset preferentially target hub regions.[2] Nonetheless, many animal experiments confirm that pathogenic alpha-synuclein does propagate via anatomical connections.[8–10] Several human imaging studies, including this one, also support the model.[2,11,65,91,94,99]

Atrophy progression-related genes are enriched for mitochondrial and metabolic function

Cortical atrophy progression was associated with gene expression profiles enriched for mitochondrial and metabolic function. Mitochondrial dysfunction was first implicated in PD based on the observation that exposure to the drug 1-methyl-4-phenyl-1,2,3,4-tetrahydropyridine (MPTP) induced the rapid onset of parkinsonism and degeneration in the substantia nigra of humans.[102,103] Further inspection revealed this toxic effect was mediated by the inhibition of complex I of the mitochondrial electron transport chain. But even in cases of sporadic PD, reductions in complex I activity within the substantia nigra as well as in the cortex and periphery have been reported.[104–106] Interestingly, we identified NADH dehydrogenase complex as one of the most enriched terms in our GSEA. Specific genetic mutations in PD-related genes such as PINK and Parkin have also been implicated in defective mitochondrial function and regulation through impaired mitophagy of damaged mitochondria.[107–110] Impaired mitochondria produce less cellular energy, but more reactive oxygen species linked to oxidative stress. The accumulation of dysfunctional mitochondria may contribute to regional vulnerability to PD pathology. Moreover, mitochondrial failure and accumulation of misfolded alpha-synuclein may promote each

other in a bi-directional fashion.[111] Our results add to this view by showing that cortical areas with more mitochondria-related gene expression are especially vulnerable to atrophy progression in PD. We also replicated findings from a previous study in prodromal PD patients that showed cortical atrophy-related genes were enriched for mitochondrial function.[98]

Limitations

We examined *de novo* PD patients followed longitudinally over a 4-year duration. This within-subject, multiple time point design afforded us control of the large between-subject variability due to disease heterogeneity and a broader view of disease progression. Despite these advantages, this approach presents a few challenges. First, not all PD patients had MRI data available at all four visits due to either scans failing quality control for a subset of time points or because of attrition which is common among longitudinal studies. We therefore included only those individuals with data available at two or more time points and employed linear mixed effects modeling, which is robust to data with irregular timing and subject drop-out.[33] Next, although we examined PD patients over more frequent visits and across a longer span than most previous studies, still our results only reveal progression over an early and narrow window relative to the PD course. Modeling repeated visits over a longer duration would allow for a more precise and accurate estimation of brain trajectories. This approach would also better capture cortical changes and accompanying cognitive deficits presumed to be most pronounced later in the disease course.

Cortical thinning was used as a proxy for PD pathology. At present, direct measures of alpha-synuclein distribution in PD patients *in vivo* are not possible as there are yet to exist validated PET radiotracers for this protein. Such a tracer would allow for more accurate study of disease spread, as has been demonstrated in the case of beta-amyloid and tauopathies such as Alzheimer's disease and frontotemporal dementia.[112,113] Still, brain atrophy measured with MRI can arguably be used as an indirect surrogate of alpha-synuclein pathology in the brain.

The PPMI dataset consists of clinical and imaging data contributed from multiple centres and scanners, which might introduce unwanted heterogeneity.[114] However, the PPMI has strict and standardized protocols for data acquisition[22] and the CIVET pipeline used for analyzing cortical thickness in the present study was developed and validated to deal with such multi-centre datasets.[115] Further, we include scanning site as a covariate in our analyses of cortical atrophy and clinical progression.

Conclusion

In summary, the present study reveals a distinct pattern of cortical atrophy progression across the early stage of PD. This pattern appears to be shaped by structural and functional network architecture as well as regional differences in factors such as cellular composition, neuroreceptor distribution, and gene expression. Notably, the gene expression profiles related to atrophy progression are associated with mitochondrial and metabolic functions. These results demonstrate how both global network and local vulnerability factors shape the progression of cortical atrophy in PD.

Acknowledgements

PPMI—a public-private partnership—is funded by the Michael J. Fox Foundation for Parkinson's Research and funding partners, including AbbVie, Avid, Biogen, Bristol-Myers Squibb, Covance, GE Healthcare, Genentech, GlaxoSmithKline, Lilly, Lundbeck, Merck, Meso Scale Discovery, Pfizer, Piramal, Sanofi Genzyme, Servier, Teva, and UCB. This research was supported by grants from the Michael J. Fox Foundation for Parkinson's Research, the W. Garfield Weston Foundation, the Alzheimer's Association, the Canadian Institutes of Health Research, and the Natural Sciences and Engineering Research Council of Canada to AD. AV acknowledges support from Frontiers de Recherche du Quebec – Santé. SR received a scholarship from the Canada Institutes of Health Research.

References

1. Mak, E. *et al.* Baseline and longitudinal grey matter changes in newly diagnosed Parkinson's disease: ICICLE-PD study. *Brain* 138, 2974–2986 (2015).

2. Zeighami, Y. *et al.* Network structure of brain atrophy in de novo Parkinson's disease. *Elife* 4, e08440 (2015).

3. Sterling, N. W. *et al.* Stage-dependent loss of cortical gyrification as Parkinson disease "unfolds." *Neurology* 86, 1143–1151 (2016).

4. Braak, H. *et al.* Staging of brain pathology related to sporadic Parkinson's disease. *Neurobiol Aging* 24, 197–211 (2003).

5. Braak, H., Rüb, U. & Tredici, K. D. Cognitive decline correlates with neuropathological stage in Parkinson's disease. *J Neurol Sci* 248, 255–258 (2006).

6. Seeley, W. W., Crawford, R. K., Zhou, J., Miller, B. L. & Greicius, M. D. Neurodegenerative Diseases Target Large-Scale Human Brain Networks. *Neuron* 62, 42–52 (2009).

7. Warren, J. D. *et al.* Molecular nexopathies: a new paradigm of neurodegenerative disease. *Trends Neurosci* 36, 561–569 (2013).

8. Masuda-Suzukake, M. *et al.* Prion-like spreading of pathological α-synuclein in brain. *Brain* 136, 1128–1138 (2013).

9. Mougenot, A.-L. *et al.* Prion-like acceleration of a synucleinopathy in a transgenic mouse model. *Neurobiol Aging* 33, 2225–2228 (2012).

10. Luk, K. C. *et al.* Pathological α-Synuclein Transmission Initiates Parkinson-like Neurodegeneration in Nontransgenic Mice. *Science* 338, 949–953 (2012).

11. Yau, Y. *et al.* Network connectivity determines cortical thinning in early Parkinson's disease progression. *Nat Commun* 9, 12 (2018).

12. Borghammer, P. & Berge, N. V. D. Brain-First versus Gut-First Parkinson's Disease: A Hypothesis. *J Park Dis* 9, S281–S295 (2019).

13. Surmeier, D. J., Obeso, J. A. & Halliday, G. M. Parkinson's Disease Is Not Simply a Prion Disorder. *J Neurosci* 37, 9799–9807 (2017).

14. Gonzalez-Rodriguez, P., Zampese, E. & Surmeier, D. J. Selective neuronal vulnerability in Parkinson's disease. *Prog Brain Res* 252, 61–89 (2020).

15. Wei, Y., Scholtens, L. H., Turk, E. & Heuvel, M. P. van den. Multiscale examination of cytoarchitectonic similarity and human brain connectivity. *Netw Neurosci* 3, 124–137 (2018).

16. Hansen, J. Y. *et al.* Local molecular and global connectomic contributions to cross-disorder cortical abnormalities. *Nat Commun* 13, 4682 (2022).

17. Arnatkevičiūtė, A., Fulcher, B. D. & Fornito, A. Uncovering the Transcriptional Correlates of Hub Connectivity in Neural Networks. *Front Neural Circuit* 13, 47 (2019).

18. Luna, E. *et al.* Differential α-synuclein expression contributes to selective vulnerability of hippocampal neuron subpopulations to fibril-induced toxicity. *Acta Neuropathol* 135, 855–875 (2018).

19. Zheng, Y.-Q. *et al.* Local vulnerability and global connectivity jointly shape neurodegenerative disease propagation. *Plos Biol* 17, e3000495 (2019).

20. Rahayel, S. *et al.* Brain atrophy in prodromal synucleinopathy is shaped by structural connectivity and gene expression. *Brain* 145, 3162–3178 (2022).

21. Rahayel, S. *et al.* Differentially targeted seeding reveals unique pathological alpha-synuclein propagation patterns. *Brain* awab440- (2021) doi:10.1093/brain/awab440.

22. Marek, K. *et al.* The Parkinson Progression Marker Initiative (PPMI). *Prog Neurobiol* 95, 629–635 (2011).

23. Shafiei, G. *et al.* Network structure and transcriptomic vulnerability shape atrophy in frontotemporal dementia. *Brain* awac069 (2022) doi:10.1093/brain/awac069.

24. Shafiei, G. *et al.* Spatial Patterning of Tissue Volume Loss in Schizophrenia Reflects Brain Network Architecture. *Biol Psychiat* 87, 727–735 (2019).

25. Association, W. M. World Medical Association Declaration of Helsinki: Ethical Principles for Medical Research Involving Human Subjects. *Jama* 310, 2191–2194 (2013).

26. Ad-Dab'bagh, Y. *et al.* The CIVET image-processing environment: a fully automated comprehensive pipeline for anatomical neuroimaging research. in vol. 2266 (Florence, Italy).

27. Fonov, V. *et al.* Unbiased average age-appropriate atlases for pediatric studies. *Neuroimage* 54, 313–327 (2011).

28. Fonov, V., Evans, A., McKinstry, R., Almli, C. & Collins, D. Unbiased nonlinear average age-appropriate brain templates from birth to adulthood. *Neuroimage* 47, S102 (2009).

29. Kim, J. S. *et al.* Automated 3-D extraction and evaluation of the inner and outer cortical surfaces using a Laplacian map and partial volume effect classification. *Neuroimage* 27, 210–221 (2005).

30. Joie, R. L. *et al.* Prospective longitudinal atrophy in Alzheimer's disease correlates with the intensity and topography of baseline tau-PET. *Sci Transl Med* 12, eaau5732 (2020).

31. Desikan, R. S. *et al.* An automated labeling system for subdividing the human cerebral cortex on MRI scans into gyral based regions of interest. *Neuroimage* 31, 968–980 (2006).

32. Cammoun, L. *et al.* Mapping the human connectome at multiple scales with diffusion spectrum MRI. *J Neurosci Meth* 203, 386–397 (2012).

33. Bernal-Rusiel, J. L. *et al.* Statistical analysis of longitudinal neuroimage data with Linear Mixed Effects models. *Neuroimage* 66, 249–260 (2013).

34. McIntosh, A. R. & Lobaugh, N. J. Partial least squares analysis of neuroimaging data: applications and advances. *Neuroimage* 23, S250–S263 (2004).

35. Krishnan, A., Williams, L. J., McIntosh, A. R. & Abdi, H. Partial Least Squares (PLS) methods for neuroimaging: A tutorial and review. *Neuroimage* 56, 455–475 (2011).

36. Eckart, C. & Young, G. The approximation of one matrix by another of lower rank. *Psychometrika* 1, 211–218 (1936).

37. Alexander-Bloch, A. F. *et al.* On testing for spatial correspondence between maps of human brain structure and function. *Neuroimage* 178, 540–551 (2018).

38. Markello, R. D. & Misic, B. Comparing spatial null models for brain maps. *Neuroimage* 236, 118052 (2021).

39. Váša, F. & Mišić, B. Null models in network neuroscience. *Nat Rev Neurosci* 23, 493–504 (2022).

40. Yeo, B. T. T. *et al.* The organization of the human cerebral cortex estimated by intrinsic functional connectivity. *J Neurophysiol* 106, 1125–1165 (2011).

41. Economo, C. F. von & Koskinas, G. N. *Die cytoarchitektonik der hirnrinde des erwachsenen menschen*. (J. Springer, 1925).

42. Scholtens, L. H., Reus, M. A. de, Lange, S. C. de, Schmidt, R. & Heuvel, M. P. van den. An MRI Von Economo – Koskinas atlas. *Neuroimage* 170, 249–256 (2018).

43. Seidlitz, J. *et al.* Transcriptomic and cellular decoding of regional brain vulnerability to neurogenetic disorders. *Nat Commun* 11, 3358 (2020).

44. Shin, J. *et al.* Cell-Specific Gene-Expression Profiles and Cortical Thickness in the Human Brain. *Cereb Cortex* 28, 3267–3277 (2017).

45. Markello, R. D. *et al.* neuromaps: structural and functional interpretation of brain maps. *Nat Methods* 1–8 (2022) doi:10.1038/s41592-022-01625-w.

46. Hansen, J. Y. *et al.* Mapping neurotransmitter systems to the structural and functional organization of the human neocortex. *Nat Neurosci* 1–13 (2022) doi:10.1038/s41593-022-01186-3.

47. Hawrylycz, M. J. *et al.* An anatomically comprehensive atlas of the adult human brain transcriptome. *Nature* 489, 391–399 (2012).

48. Markello, R. D. *et al.* Standardizing workflows in imaging transcriptomics with the abagen toolbox. *Elife* 10, (2021).

49. Arnatkevičiūtė, A., Fulcher, B. D. & Fornito, A. A practical guide to linking brain-wide gene expression and neuroimaging data. *Neuroimage* 189, 353–367 (2019).

50. Griffa, A., Alemán-Gómez, Y. & Hagmann, P. Structural and functional connectome from 70 young healthy adults [Data set]. *Zenodo* (2019) doi:10.5281/zenodo.2872624.

51. Betzel, R. F., Griffa, A., Hagmann, P. & Mišić, B. Distance-dependent consensus thresholds for generating group-representative structural brain networks. *Netw Neurosci* 3, 475–496 (2019).

52. Shafiei, G., Baillet, S. & Misic, B. Human electromagnetic and haemodynamic networks systematically converge in unimodal cortex and diverge in transmodal cortex. *Plos Biol* 20, e3001735 (2022).

53. Romero-Garcia, R. *et al.* Structural covariance networks are coupled to expression of genes enriched in supragranular layers of the human cortex. *Neuroimage* 171, 256–267 (2018).

54. Petrican, R., Fornito, A. & Jones, N. Psychological resilience and neurodegenerative risk: A connectomics-transcriptomics investigation in healthy adolescent and middle-aged females. *Neuroimage* 255, 119209 (2022).

55. Fulcher, B. D. & Fornito, A. A transcriptional signature of hub connectivity in the mouse connectome. *Proc National Acad Sci* 113, 1435–1440 (2016).

56. Liao, Y., Wang, J., Jaehnig, E. J., Shi, Z. & Zhang, B. WebGestalt 2019: gene set analysis toolkit with revamped UIs and APIs. *Nucleic Acids Res* 47, W199–W205 (2019).

57. Subramanian, A. *et al.* Gene set enrichment analysis: A knowledge-based approach for interpreting genome-wide expression profiles. *Proc National Acad Sci* 102, 15545–15550 (2005).

58. *Die Cytoarchitektonik der Hirnrinde des erwachsenen Menschen. (The Cyto-Architectonics of the Cerebral Cortex of Adult Man.).* (1926).

59. Vidal-Pineiro, D. *et al.* Cellular correlates of cortical thinning throughout the lifespan. *Sci Rep-uk* 10, 21803 (2020).

60. Laansma, M. A. *et al.* International Multicenter Analysis of Brain Structure Across Clinical Stages of Parkinson's Disease. *Movement Disord* 2020.04.28.20072710 (2020) doi:10.1002/mds.28706.

61. Uribe, C. *et al.* Patterns of cortical thinning in nondemented Parkinson's disease patients. *Movement Disord* 31, 699–708 (2016).

62. Uribe, C. *et al.* Cortical atrophy patterns in early Parkinson's disease patients using hierarchical cluster analysis. *Parkinsonism Relat Disord* 50, 3–9 (2018).

63. Pereira, J. B. *et al.* Initial cognitive decline is associated with cortical thinning in early Parkinson disease. *Neurology* 82, 2017–2025 (2014).

64. Uribe, C. *et al.* Progression of Parkinson's disease patients' subtypes based on cortical thinning: 4-year follow-up. *Parkinsonism Relat D* 64, 286–292 (2019).

65. Tremblay, C. *et al.* Brain atrophy progression in Parkinson's disease is shaped by connectivity and local vulnerability. *Brain Commun* 3, fcab269 (2021).

66. Abdelgawad, A. *et al.* Predicting longitudinal brain atrophy in Parkinson's disease using a Susceptible-Infected-Removed agent-based model. *Netw Neurosci* 1–20 (2023) doi:10.1162/netn_a_00296.

67. Zhao, Y. J. *et al.* Progression of Parkinson's disease as evaluated by Hoehn and Yahr stage transition times. *Mov. Disord.* 25, 710–716 (2010).

68. Fereshtehnejad, S.-M. *et al.* New Clinical Subtypes of Parkinson Disease and Their Longitudinal Progression: A Prospective Cohort Comparison With Other Phenotypes. *Jama Neurol* 72, 863–873 (2015).

69. Zeighami, Y. *et al.* A clinical-anatomical signature of Parkinson's disease identified with partial least squares and magnetic resonance imaging. *Neuroimage* 190, 69–78 (2019).

70. Irwin, D. J. *et al.* Neuropathologic substrates of Parkinson disease dementia. *Ann Neurol.* 72, 587–598 (2012).

71. Irwin, D. J. *et al.* Evolution of Alzheimer's Disease Cerebrospinal Fluid Biomarkers in Early Parkinson's Disease. *Ann Neurol* 88, 574–587 (2020).

72. O'Keeffe, G. W. & Sullivan, A. M. Evidence for dopaminergic axonal degeneration as an early pathological process in Parkinson's disease. *Parkinsonism Relat D* 56, 9–15 (2018).

73. Khalil, M. *et al.* Neurofilaments as biomarkers in neurological disorders. *Nat Rev Neurol* 14, 577–589 (2018).

74. Gafson, A. R. *et al.* Neurofilaments: neurobiological foundations for biomarker applications. *Brain* 143, 1975–1998 (2020).

75. Aamodt, W. W. *et al.* Neurofilament Light Chain as a Biomarker for Cognitive Decline in Parkinson Disease. *Movement Disord* 36, 2945–2950 (2021).

76. Mollenhauer, B. *et al.* Validation of Serum Neurofilament Light Chain as a Biomarker of Parkinson's Disease Progression. *Mov. Disord.* 35, 1999–2008 (2020).

77. Bäckström, D. *et al.* NfL as a biomarker for neurodegeneration and survival in Parkinson disease. *Neurology* 95, 10.1212/WNL.0000000000010084 (2020).

78. Ye, R. *et al.* Serum NFL levels predict progression of motor impairment and reduction in putamen dopamine transporter binding ratios in de novo Parkinson's disease: An 8-year longitudinal study. *Parkinsonism Relat D* 85, 11–16 (2021).

79. Kish, S. J., Shannak, K. & Hornykiewicz, O. Uneven Pattern of Dopamine Loss in the Striatum of Patients with Idiopathic Parkinson's Disease. *New Engl J Medicine* 318, 876–880 (1988).

80. Smethurst, P., Franklin, H., Clarke, B. E., Sidle, K. & Patani, R. The role of astrocytes in prion-like mechanisms of neurodegeneration. *Brain* (2022) doi:10.1093/brain/awab366.

81. Cavaliere, F. *et al.* In vitro α-synuclein neurotoxicity and spreading among neurons and astrocytes using Lewy body extracts from Parkinson disease brains. *Neurobiol Dis* 103, 101–112 (2017).

82. He-Jin, L., Changyoun, K. & Seung-Jae, L. Alpha-Synuclein Stimulation of Astrocytes: Potential Role for Neuroinflammation and Neuroprotection. *Oxid Med Cell Longev* 3, 283–287 (2010).

83. Loria, F. *et al.* α-Synuclein transfer between neurons and astrocytes indicates that astrocytes play a role in degradation rather than in spreading. *Acta Neuropathol* 134, 789–808 (2017).

84. Rinne, J. O. *et al.* Increased brain histamine levels in Parkinson's disease but not in multiple system atrophy. *J Neurochem* 81, 954–960 (2002).

85. Brotchie, J. M. CB1 cannabinoid receptor signalling in Parkinson's disease. *Curr Opin Pharmacol* 3, 54–61 (2003).

86. Anichtchik, O. V., Peitsaro, N., Rinne, J. O., Kalimo, H. & Panula, P. Distribution and Modulation of Histamine H3 Receptors in Basal Ganglia and Frontal Cortex of Healthy Controls and Patients with Parkinson's Disease. *Neurobiol Dis* 8, 707–716 (2001).

87. Bezard, E. *et al.* μ Opioid Receptor Agonism for L-DOPA-Induced Dyskinesia in Parkinson's Disease. *J Neurosci* 40, 6812–6819 (2020).

88. Politis, M. *et al.* Depressive symptoms in PD correlate with higher 5-HTT binding in raphe and limbic structures. *Neurology* 75, 1920–1927 (2010).

89. Kish, S. J., Shannak, K., Rajput, A., Deck, J. H. N. & Hornykiewicz, O. Aging Produces a Specific Pattern of Striatal Dopamine Loss: Implications for the Etiology of Idiopathic Parkinson's Disease. *J Neurochem* 58, 642–648 (1992).

90. Zhou, J., Gennatas, E. D., Kramer, J. H., Miller, B. L. & Seeley, W. W. Predicting Regional Neurodegeneration from the Healthy Brain Functional Connectome. *Neuron* 73, 1216–1227 (2012).

91. Pandya, S. *et al.* Predictive model of spread of Parkinson's pathology using network diffusion. *Neuroimage* 192, 178–194 (2019).

92. Meier, J. M. *et al.* Connectome-Based Propagation Model in Amyotrophic Lateral Sclerosis. *Ann Neurol* 87, 725–738 (2020).

93. Polymenidou, M. & Cleveland, D. W. The Seeds of Neurodegeneration: Prion-like Spreading in ALS. *Cell* 147, 498–508 (2011).

94. Raj, A., Kuceyeski, A. & Weiner, M. A Network Diffusion Model of Disease Progression in Dementia. *Neuron* 73, 1204–1215 (2012).

95. Fornari, S., Schäfer, A., Jucker, M., Goriely, A. & Kuhl, E. Prion-like spreading of Alzheimer's disease within the brain's connectome. *J Roy Soc Interface* 16, 20190356 (2019).

96. Jucker, M. & Walker, L. C. Self-propagation of pathogenic protein aggregates in neurodegenerative diseases. *Nature* 501, 45–51 (2013).

97. Frost, J. J. *et al.* Positron emission tomographic imaging of the dopamine transporter with 11C-WIN 35,428 reveals marked declines in mild Parkinson's disease. *Ann Neurol* 34, 423–431 (1993).

98. Rahayel, S. *et al.* Mitochondrial function-associated genes underlie cortical atrophy in prodromal synucleinopathies. *Brain* (2023) doi:10.1093/brain/awad044.

99. Maia, P. D. *et al.* Origins of atrophy in Parkinson linked to early onset and local transcription patterns. *Brain Commun* 2, fcaa065- (2020).

100. Crossley, N. A. *et al.* The hubs of the human connectome are generally implicated in the anatomy of brain disorders. *Brain* 137, 2382–2395 (2014).

101. Heuvel, M. P. van den & Sporns, O. Rich-Club Organization of the Human Connectome. *J Neurosci* 31, 15775–15786 (2011).

102. Langston, J. W., Ballard, P., Tetrud, J. W. & Irwin, I. Chronic Parkinsonism in Humans Due to a Product of Meperidine-Analog Synthesis. *Science* 219, 979–980 (1983).

103. Langston, J. W. & Jr, P. A. B. Parkinson's disease in a chemist working with l-methyl-4-phenyl-1,2,5,6-tetrahydropyridine. 309,.

104. Parker, W. D., Parks, J. K. & Swerdlow, R. H. Complex I deficiency in Parkinson's disease frontal cortex. *Brain Res* 1189, 215–218 (2008).

105. Subrahmanian, N. & LaVoie, M. J. Is there a special relationship between complex I activity and nigral neuronal loss in Parkinson's disease? A critical reappraisal. *Brain Res* 1767, 147434 (2021).

106. González-Rodríguez, P. *et al.* Disruption of mitochondrial complex I induces progressive parkinsonism. *Nature* 599, 650–656 (2021).

107. Chan, P., DeLanney, L. E., Irwin, I., Langston, J. W. & Monte, D. Rapid ATP Loss Caused by 1-Methyl-4-Phenyl-1,2,3,6-Tetrahydropyridine in Mouse Brain. *J Neurochem* 57, 348–351 (1991).

108. Zhou, C., Huang, Y. & Przedborski, S. Oxidative Stress in Parkinson's Disease. *Ann Ny Acad Sci* 1147, 93–104 (2008).

109. Mahadevan, H. M., Hashemiaghdam, A., Ashrafi, G. & Harbauer, A. B. Mitochondria in Neuronal Health: From Energy Metabolism to Parkinson's Disease. *Adv Biology* 5, 2100663 (2021).

110. Blauwendraat, C., Nalls, M. A. & Singleton, A. B. The genetic architecture of Parkinson's disease. *Lancet Neurology* 19, 170–178 (2020).

111. Rocha, E. M., Miranda, B. D. & Sanders, L. H. Alpha-synuclein: Pathology, mitochondrial dysfunction and neuroinflammation in Parkinson's disease. *Neurobiol Dis* 109, 249–257 (2018).

112. Vogel, J. W. *et al.* A molecular gradient along the longitudinal axis of the human hippocampus informs large-scale behavioral systems. *Nat Commun* 11, 960 (2020).

113. Harrison, T. M. *et al.* Longitudinal tau accumulation and atrophy in aging and alzheimer disease. *Ann Neurol* 85, 229–240 (2019).

114. Grimes, D. A. & Schulz, K. F. Bias and causal associations in observational research. *Lancet* 359, 248–252 (2002).

115. Dadar, M., Fonov, V. S., Collins, D. L. & Initiative, A. D. N. A comparison of publicly available linear MRI stereotaxic registration techniques. *NeuroImage* 174, 191–200 (2018).

Table 1. Demographic and progression of clinical measures in Parkinson's disease patients (N = 160)

	Baseline	T-statistic	P_{FDR}
Demographic			
Age (y)	61.12 ± 9.76	-	-
Sex (M/F)	102/58	-	-
Educ (y)	15.57 ± 2.96	-	-
Duration (d)	214.50 ± 224.74	-	-
Disease severity			
H&Y stage	1.58 ± 0.53	3.785	<0.001*
Motor			
MDS-UPDRS-II	5.05 ± 4.21	8.016	<0.001*
MDS-UPDRS-III (total)	19.12 ± 8.58	4.394	<0.001*
MDS-UPDRS-III (tremor)	2.90 ± 2.85	2.822	0.010*
MDS-UPDRS-III (rigidity)	3.75 ± 2.63	5.884	<0.001*
Non-motor			
MDS-UPDRS-I	4.38 ± 3.97	8.413	<0.001*
RBDSQ	3.90 ± 2.58	2.705	0.014*
SCOPA-AUT	8.94 ± 5.80	5.258	<0.001*
MoCA	27.40 ± 2.23	0.506	0.639
Phonemic fluency	13.27 ± 4.26	3.181	0.004*
Semantic fluency	21.30 ± 4.87	1.857	0.100
SDMT	41.89 ± 10.06	-0.769	0.502
HVLT (total recall)	24.89 ± 5.12	-0.253	0.800
HVLT (recognition)	10.98 ± 1.49	1.976	0.081
HVLT (delayed recall)	8.37 ± 2.65	0.949	0.429
LNS	10.99 ± 2.45	-0.905	0.436
Benton JLO	25.88 ± 4.14	1.997	0.081
QUIP	0.33 ± 0.71	1.120	0.347
Mood			
GDS	0.94 ± 1.20	1.794	0.108
STAI	88.40 ± 16.14	0.734	0.504
CSF (pg/mL)			
Alpha-synuclein	1426.60 ± 579.50	-1.305	0.267
Beta-amyloid	868.82 ± 299.75	-9.412	<0.001*
p-tau	14.29 ± 4.25	-8.861	<0.001*
t-tau	165.63 ± 47.63	-8.403	<0.001*
NfL	12.16 ± 5.76	3.387	0.002*

Age = age in years; Sex = male to female ratio; Edu = education in years; Duration = number of days since diagnosis; H&Y stage = Hoehn and Yahr stage score; UPDRS = Unified Parkinson's Disease Rating Scale; UPDRS-I = score on Part I (Mentation, Behavior, Mood) of the UPDRS; UPDRS-II = score on Part II (Activities of Daily Living) of the UPDRS; UPDRS-III = score on Part III (Motor Examination) of the UPDRS; Tremor = tremor score on the UPDRS-III; Rigidity = rigidity score on the UPDRS-III; RBDSQ = REM Sleep Behavior Disorder Sleep Questionnaire score; SCOPA-AUT = Scales for Outcomes in PArkinson's disease-Autonomic Dysfunction score; MOCA = Montreal Cognitive Assessment score; Phonemic fluency = number of words beginning with the letter 'F' listed in 1 minute; Semantic fluency = number of category items listed in 1 minute; SDMT = Symbol Digit Modalities Test score; HVLT = Hopkins Verbal Learning

Test-Revised score; LNS = Letter-Number Sequencing test score; Benton JLO = Benton Judgement of Line Orientation test score; QUIP = Questionnaire for Impulsive-Compulsive Disorders score; GDS = Geriatric Depression Scale score; STAI = State Trait Anxiety Inventory score; p-tau = phosphorylated tau; t-tau = total tau; NfL = neurofilament light chain

Figure Legends

Figure 1. Pattern of cortical atrophy rates in Parkinson's disease. (a) Rates of cortical thickness changes across longitudinal follow-up visits in PD patients **(b)** in regions with significant time effects after FDR-correction for multiple comparisons ($p_{FDR} < 0.05$).

Figure 2. Atrophy-clinical progression relationship. (a) Brain loadings (i.e., bootstrap ratios) associated with the first significant latent variable from a partial least squares analysis between individual patient atrophy rates and clinical variable progression. Bluer regions represent more positive contribution to the expression of the atrophy-clinical latent variable. **(b)** Scatterplot of the correlation between brain loadings and atrophy rates. **(c)** Clinical variable loadings associated with the first significant latent variable. Blue boxes indicate clinical variables that significantly contributed to the latent variable. Error bars represent 95% confidence intervals.

Figure 3. Distribution of cortical atrophy progression within different brain systems. (a) Boxplot of the mean atrophy rates within intrinsic resting networks (vis = visual, sm = sensorimotor, da = dorsal attention, va = ventral attention, lim = limbic, fp = frontoparietal, dmn = default mode) and **(b)** cytoarchitectonic classes (pm = primary motor, ac/ac2 = association 1/2, pss = primary/secondary sensory, ps = primary sensory, lb = limbic, ic = insular. **(c)** Boxplot of correlations between regional atrophy rates and cell type distributions (astro = astrocytes, endo = endothelial cells, ex/in = excitatory and inhibitory neurons, micro = microglia, oligo = oligodendrocytes, opc = oligodendrocyte precursors). **(d)** Boxplot of correlations between regional atrophy rates and 19 different neurochemical maps: acetylcholine ($\alpha_4\beta_2$, M_1, VAChT), cannabinoid (CB_1), dopamine (D_1, D_2, DAT), GABA ($GABA_{A/BZ}$), histamine (H_3), glutamate ($mGluR_5$, NMDA), norepinephrine (NET), opioid (MOR), and serotonin (5-HT_{1A}, 5-HT_{1B}, 5-HT_{2A}, 5-HT_4, 5-HT_6, 5-HTT). Grey boxes denote significant means or correlations when tested against spatial autocorrelation-preserving null models ($p_{spin} < 0.05$).

Figure 4. Network spreading models of cortical atrophy progression. (a) Schematic of network spreading model. Reference structural and functional connectivity networks were derived from a separate cohort of healthy subjects and the atrophy progression map generated from PD patients were used to compute neighbourhood atrophy rates—the average atrophy rate across anatomically connected neighbours weighted by structural or functional connectivity strength—for each node. **(b)** Scatterplots of the relationships between node versus neighbourhood atrophy rates for structurally (left) and functionally (right) connected neighbours. **(c)** Box plots comparing correlation coefficients (r)

for node-neighbourhood relationships for networks composed of connected versus not-connected neighbours. Grey boxes indicate statistical significance against spatial autocorrelation-preserving null models ($p_{spin} < 0.05$). Fisher's *z* tests compared connected versus not-connected *r* values.

Figure 5. Relationship between regional atrophy rates and gene expression profiles. Brain loadings for the **(a)** first and **(d)** second significant latent variables (i.e., PLS1 and PLS2, respectively) from a partial least squares analysis relating regional atrophy rates to gene expression profiles derived from the Allen Human Brain Atlas. Scatterplots of the relationship between **(b)** PLS1 and **(e)** PLS2 brain loadings and atrophy rates. Brain regions that contributed more positively to their respective latent variables and expressed more positively weighted genes also had greater atrophy rates. Enriched biological processes genes expression profiles associated with **(c)** PLS1 **(f)** PLS2. More positive enrichment scores were associated with patterns of greater atrophy rates. Darker blue and red bars indicate statistically significant enrichment scores ($p_{FDR} < 0.05$).

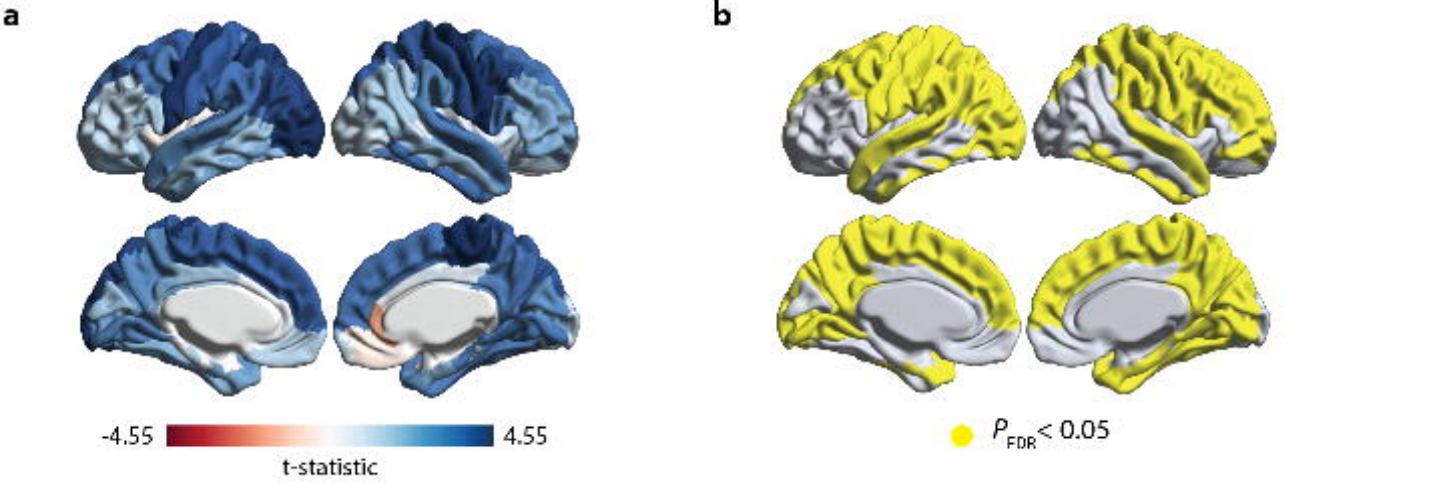
a
-4.55
4.55
t-statistic
b
$P_{FDR} < 0.05$

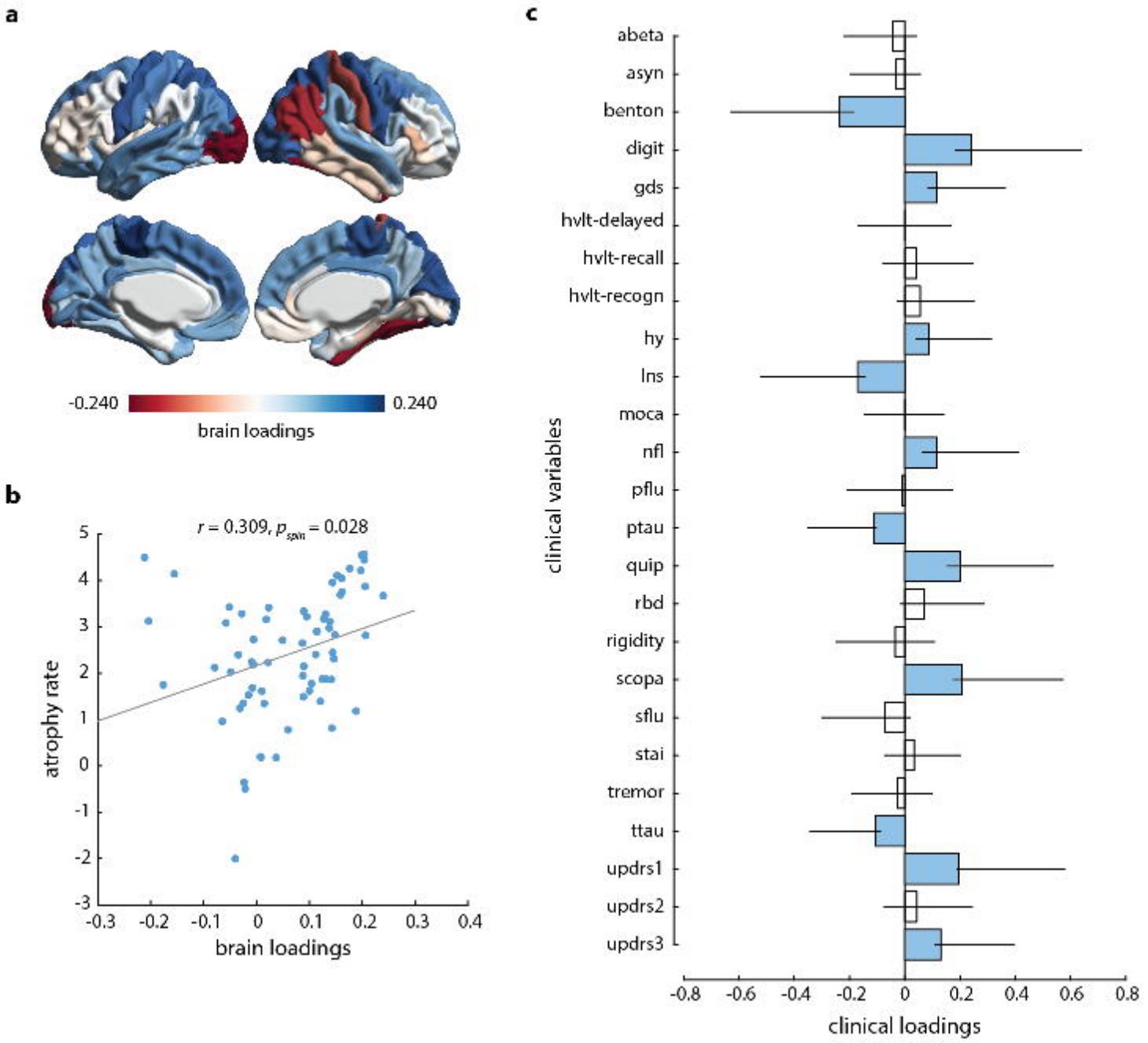
a
-0.240
0.240
brain loadings
b
r = 0.309, p_spin = 0.028
atrophy rate
brain loadings
c
abeta
asyn
benton
digit
gds
hvlt-delayed
hvlt-recall
hvlt-recogn
hy
lns
moca
nfl
pflu
ptau
quip
rbd
rigidity
scopa
sflu
stai
tremor
ttau
updrs1
updrs2
updrs3
clinical variables
clinical loadings

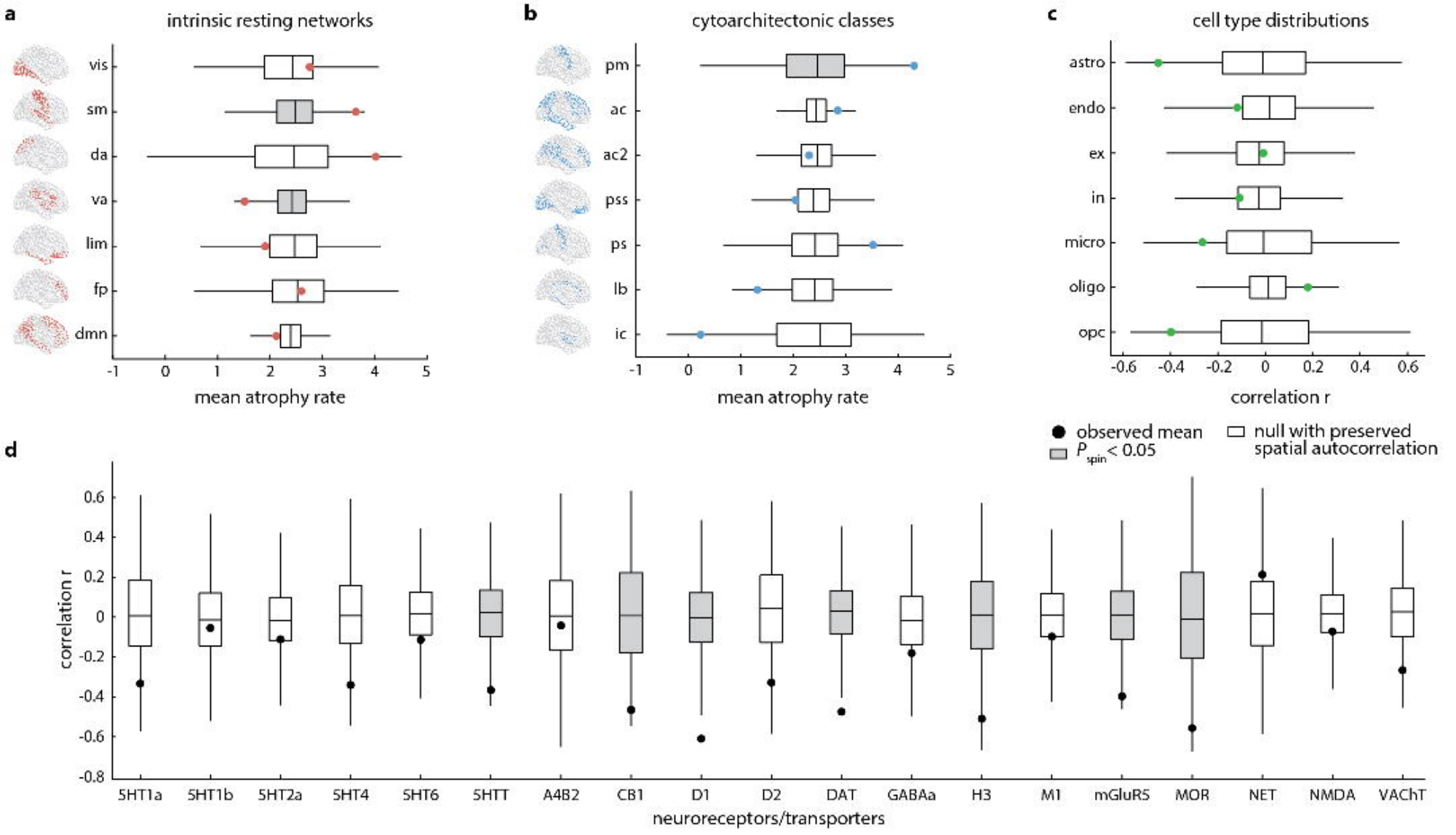
a
intrinsic resting networks
vis
sm
da
va
lim
fp
dmn
-1
0
1
2
3
4
5
mean atrophy rate
b
cytoarchitectonic classes
pm
ac
ac2
pss
ps
lb
ic
-1
0
1
2
3
4
5
mean atrophy rate
c
cell type distributions
astro
endo
ex
in
micro
oligo
opc
-0.6
-0.4
-0.2
0
0.2
0.4
0.6
correlation r
observed mean
$P_{spin} < 0.05$
null with preserved spatial autocorrelation
d
correlation r
0.6
0.4
0.2
0
-0.2
-0.4
-0.6
-0.8
5HT1a
5HT1b
5HT2a
5HT4
5HT6
5HTT
A4B2
CB1
D1
D2
DAT
GABAa
H3
M1
mGluR5
MOR
NET
NMDA
VAChT
neuroreceptors/transporters

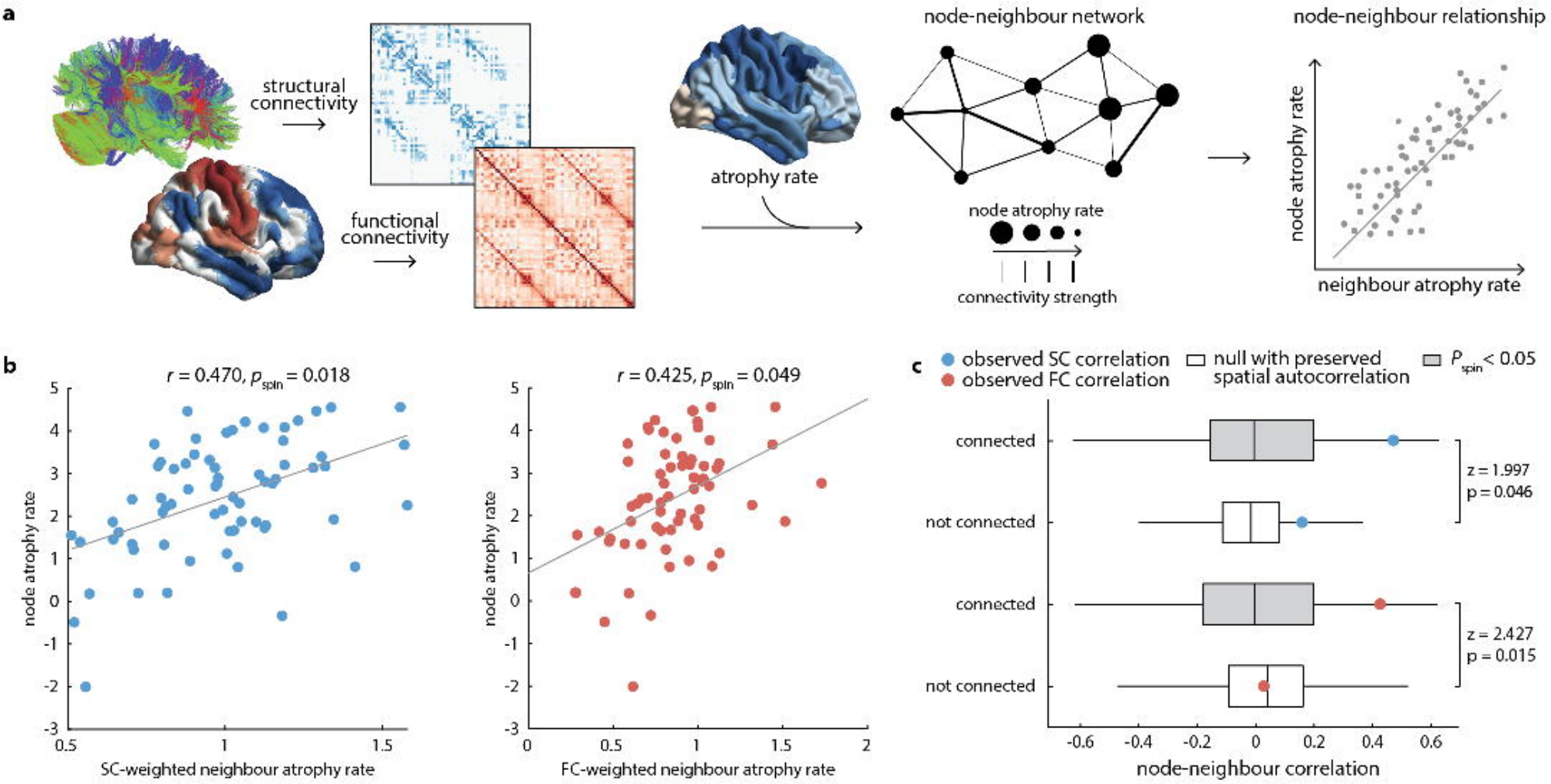
a
structural connectivity
functional connectivity
atrophy rate
node-neighbour network
node atrophy rate
connectivity strength
node-neighbour relationship
node atrophy rate
neighbour atrophy rate
b
r = 0.470, p_spin = 0.018
node atrophy rate
SC-weighted neighbour atrophy rate
r = 0.425, p_spin = 0.049
node atrophy rate
FC-weighted neighbour atrophy rate
c
observed SC correlation
observed FC correlation
null with preserved spatial autocorrelation
P_spin < 0.05
connected
not connected
connected
not connected
z = 1.997
p = 0.046
z = 2.427
p = 0.015
node-neighbour correlation

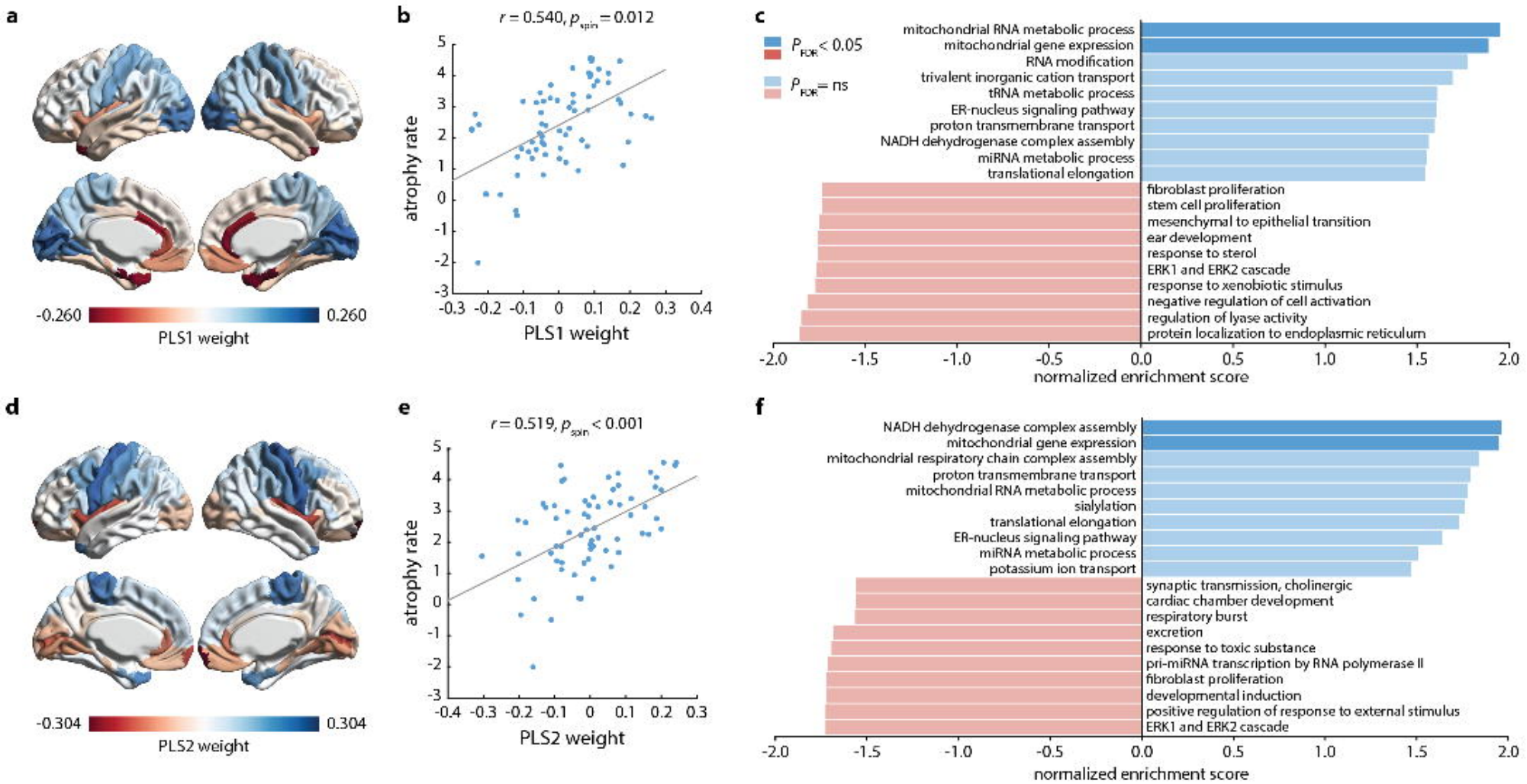
a
-0.260
0.260
PLS1 weight
b
r = 0.540, p_spin = 0.012
atrophy rate
PLS1 weight
c
P_FDR < 0.05
P_FDR = ns
mitochondrial RNA metabolic process
mitochondrial gene expression
RNA modification
trivalent inorganic cation transport
tRNA metabolic process
ER-nucleus signaling pathway
proton transmembrane transport
NADH dehydrogenase complex assembly
miRNA metabolic process
translational elongation
fibroblast proliferation
stem cell proliferation
mesenchymal to epithelial transition
ear development
response to sterol
ERK1 and ERK2 cascade
response to xenobiotic stimulus
negative regulation of cell activation
regulation of lyase activity
protein localization to endoplasmic reticulum
normalized enrichment score
d
-0.304
0.304
PLS2 weight
e
r = 0.519, p_spin < 0.001
atrophy rate
PLS2 weight
f
NADH dehydrogenase complex assembly
mitochondrial gene expression
mitochondrial respiratory chain complex assembly
proton transmembrane transport
mitochondrial RNA metabolic process
sialylation
translational elongation
ER-nucleus signaling pathway
miRNA metabolic process
potassium ion transport
synaptic transmission, cholinergic
cardiac chamber development
respiratory burst
excretion
response to toxic substance
pri-miRNA transcription by RNA polymerase II
fibroblast proliferation
developmental induction
positive regulation of response to external stimulus
ERK1 and ERK2 cascade
normalized enrichment score

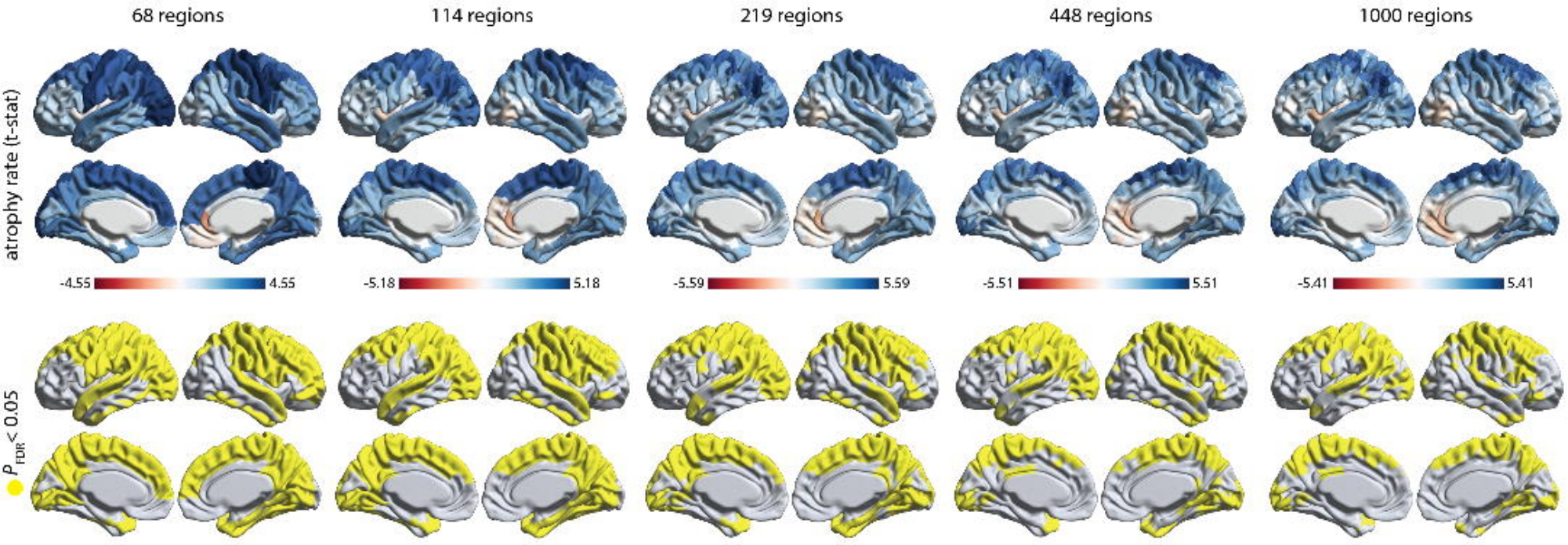
68 regions
114 regions
219 regions
448 regions
1000 regions
atrophy rate (t-stat)
-4.55
4.55
-5.18
5.18
-5.59
5.59
-5.51
5.51
-5.41
5.41
$P_{FDR} < 0.05$

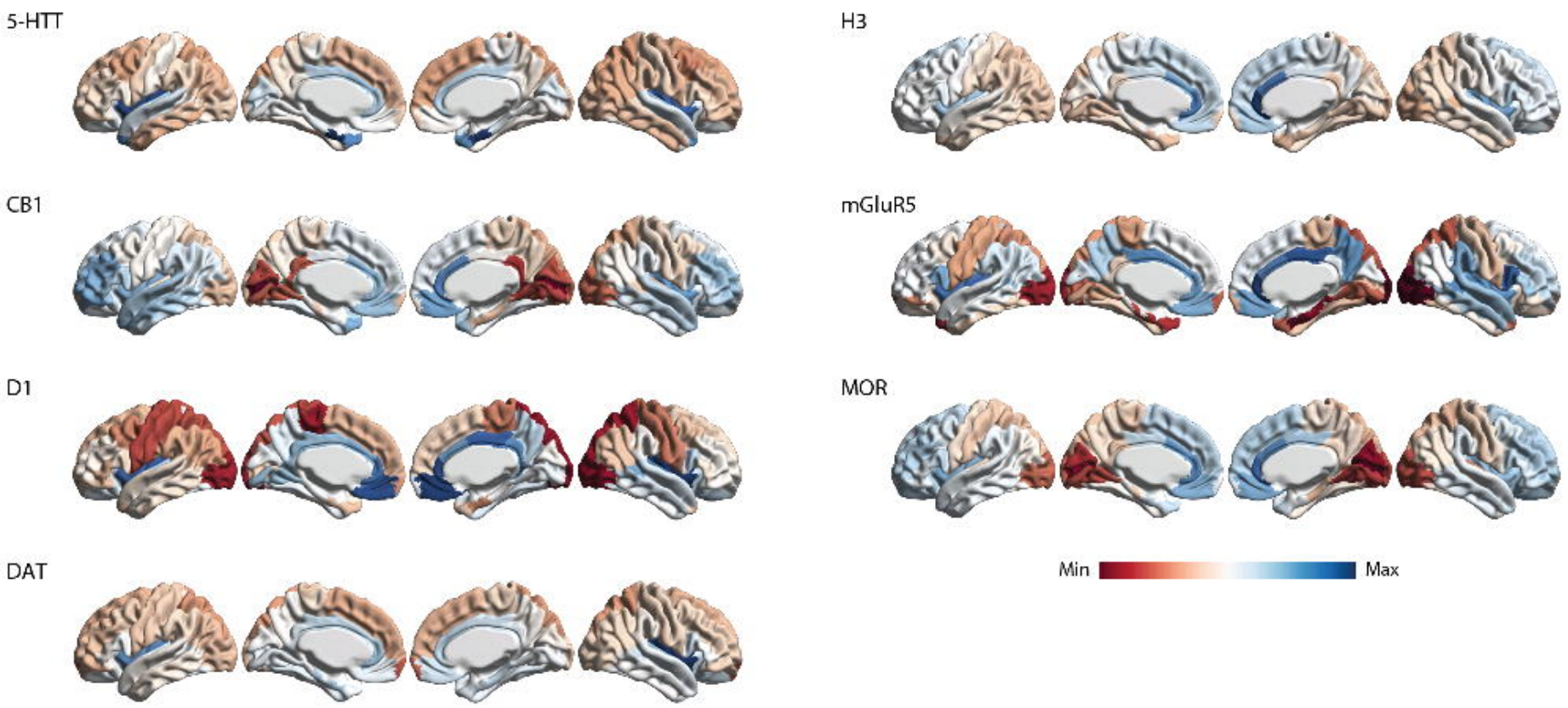
5-HTT
H3
CB1
mGluR5
D1
MOR
DAT
Min
Max

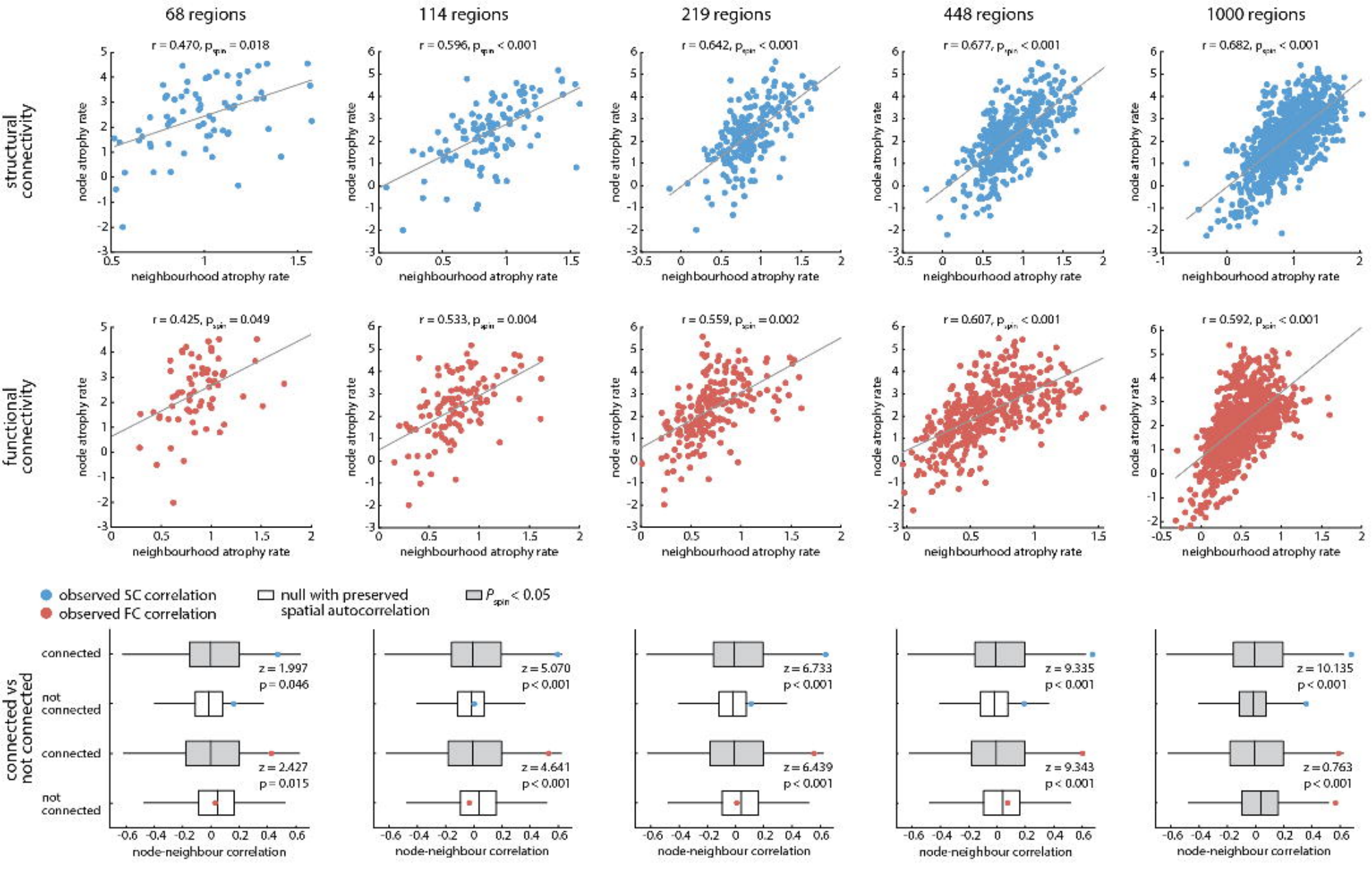
68 regions
114 regions
219 regions
448 regions
1000 regions
structural connectivity
functional connectivity
r = 0.470, p_spin = 0.018
r = 0.596, p_spin < 0.001
r = 0.642, p_spin < 0.001
r = 0.677, p_spin < 0.001
r = 0.682, p_spin < 0.001
r = 0.425, p_spin = 0.049
r = 0.533, p_spin = 0.004
r = 0.559, p_spin = 0.002
r = 0.607, p_spin < 0.001
r = 0.592, p_spin < 0.001
node atrophy rate
neighbourhood atrophy rate
observed SC correlation
observed FC correlation
null with preserved spatial autocorrelation
P_spin < 0.05
connected vs not connected
connected
not connected
z = 1.997
p = 0.046
z = 2.427
p = 0.015
z = 5.070
p < 0.001
z = 4.641
p < 0.001
z = 6.733
p < 0.001
z = 6.439
p < 0.001
z = 9.335
p < 0.001
z = 9.343
p < 0.001
z = 10.135
p < 0.001
z = 0.763
p < 0.001
node-neighbour correlation